

Article

A New Composite Control Strategy for an Astronaut Virtual Operation Training System Based on Cable-Driven Technology

Feng Xue¹, Lixun Zhang^{1,*}, Lailu Li², Zhenhan Wang¹ and Da Song³

¹ College of Mechanical and Electrical Engineering, Harbin Engineering University, No. 145, Nantong Street, Nangang District, Harbin 150009, China; crazyxuefeng@hrbeu.edu.cn (F.X.); wanghrbeu@hrbeu.edu.cn (Z.W.)

² Department of Electrical Engineering, The Chinese University of Hong Kong, Hong Kong 999077, China; lilailucn@gmail.com

³ School of Mechanical Engineering, Northeast Electric Power University, Jilin 132012, China; songda@neepu.edu.cn

* Correspondence: zhanglixun@hrbeu.edu.cn; Tel.: +86-183-4515-5805

Abstract: In recent years, virtual microgravity training technology for astronauts based on cable-driven designs has emerged, and it solves the following problems: high costs, short training times, and low safety of existing equipment. However, this technology does not solve the reduced motion accuracy problem of the operated object due to the elastic deformation of cables, and this problem will reduce the operational experience of astronauts during training. In view of this problem, a cable-driven virtual operation training system for astronauts is designed, and a new composite control strategy based on parallel cables is proposed, which effectively improves motion control accuracy by allocating cable tension and using a tension compliance control method to suppress the influence of cable deformation. In addition, the desired tension of cables is optimized based on the system's workspace so that the system can achieve more complex virtual microgravity training tasks. Finally, verification via experiments demonstrated that the training system and the new composite control strategy are effective.

Keywords: astronaut microgravity training; parallel cable drive; tension control; workspace



Citation: Xue, F.; Zhang, L.; Li, L.; Wang, Z.; Song, D. A New Composite Control Strategy for an Astronaut Virtual Operation Training System Based on Cable-Driven Technology. *Actuators* **2023**, *12*, 384. <https://doi.org/10.3390/act12100384>

Academic Editor: Zhuming Bi

Received: 2 September 2023

Revised: 5 October 2023

Accepted: 10 October 2023

Published: 12 October 2023



Copyright: © 2023 by the authors. Licensee MDPI, Basel, Switzerland. This article is an open access article distributed under the terms and conditions of the Creative Commons Attribution (CC BY) license (<https://creativecommons.org/licenses/by/4.0/>).

1. Introduction

In the weightless environment of space, the motion characteristics and mechanical properties of objects are very different from those in the Earth's gravitational environment [1]. An astronaut's senses in the process of carrying objects and installing equipment are also different compared to the experience within the terrestrial gravitational environment [2]. Due to the inability to feel gravity during the process of moving objects and disassembling and assembling equipment, the motion of objects can result in collision and damage to the equipment and even cause harm to the astronauts, such as tearing inflicted upon the spacesuit [3]. Therefore, it is necessary to train astronauts to move differently sized mass objects in a weightless environment in order to improve their object maneuverability, operational ability, and operational level and avoid the danger of collisions.

Space environments are simulated on the surface of the Earth: that is, a virtual gravitational environment is used to train astronauts. Currently, there are mainly two typical methods [4]: the motion method and the force balance method. The motion method includes the parabolic flight method and the falling tower method: for example, NASA's parabolic flight training in the United States, Germany's Bremen drop tower device [5], etc. The simulations with the parabolic flight method and falling tower method provide high-precision results, but there are problems, such as short training times, long preparation times, and high costs. The force balance method includes the air flotation method, magnetic flotation method, neutral pool method, and suspension method. Air flotation can accurately simulate the planar motion of an object in a low-gravity environment [6]. Zhou, ML et al.

designed a microgravity simulator based on air flotation [7]. In the European Space Agency (ESA) GBF project, a magnetic suspension virtual microgravity experiment was conducted using a 17 t superconducting magnet from the University of Nottingham [8]. However, the air flotation method cannot achieve microgravity simulations with 6 degrees of freedom (hereinafter referred to as DOF) in space. The neutral pool method is the most widely used. Sun et al. designed a microgravity test bench with 6 DOF [9]. Wang, T et al. analyzed the dynamics of an underwater cable drive system [10]. However, the simulation accuracy is not high due to liquid resistance [11]. The passive suspension method is simple, stable, and reliable. For example, the SM2 space mode robot was designed by Carnegie Mellon University. However, due to the resistance of the mechanical structure, there is the problem of poor simulation accuracy. The simulation accuracy of the active suspension method is high, but an active suspension system with more than 3 DOF has complex structures, occupies a large space, and is very costly [12].

To address the shortcomings of the typical virtual microgravity training methods above, a virtual microgravity training method based on a cable-driven design has emerged in recent years. The specific method is to use a cable to suspend the object and a servo system to drive the cable's movement to offset the gravity of the object and actively control the position and posture of the object (the controlled object). Then, the object conforms to the movement law in the microgravity environment [13]. The advantages of this method are as follows: high safety, small equipment volume, and larger working space; moreover, the mass and volume of transported objects can be arbitrarily set [14]. Currently, mature cable-driven virtual operation training equipment includes the four-dimensional virtual operation robot designed by Laval University in Canada, which has 3 DOF [15]; and Mini-IPAnena3, which is studied by the Fraunhofer Institute of Manufacturing Engineering and Automation for force perception interaction training with virtual environments [16]. The Charlotte robot was developed by NASA and uses VR technology and a cable drive mechanism to realize 6 DOF. VR technology builds the virtual space environment, enabling the astronauts to interact with the virtual environment via vision. VR technology increases the sense of presence and immersion during training [17]. Currently, there are two control strategies used in virtual microgravity training equipment based on cable drive systems: the cable tension control strategy and the hybrid force position control strategy [18–20]. The principle of the cable tension control strategy is that all cables are controlled by a force servo, and the desired motion law is realized by controlling the resultant force acting on the end effector. Zou, YP designed an astronaut training system and analyzed the stiffness of the cable drive system [21]. The team that the author was a member of conducted research on cable-driven on-orbit physical exercise equipment for astronauts [22]. However, the control strategy exhibits poor motion accuracy with respect to the end effector because the control object is force rather than motion. The principle of the force–position hybrid control strategy is to realize the motion control of the end effector by controlling a part of the cable's displacement. Moreover, the tension of all cables is achieved by controlling the tension of another part of the cable [23]. The force–position hybrid control strategy solves the problems that exist in the cable tension control strategy. Currently, the results of using this control strategy mainly include a four-cable system designed by Fortin-Cote, which further improves safety [24]. Park et al. proposed a small remote-operated tactile device based on a cable-driven robot to realize the synchronous motion of master and slave devices [25]. The team that the author participated in has optimized the structure of cable-driven robots, and tension distribution and speed-planning algorithms of a high-order dynamic were proposed [26,27]. The operational feeling of astronauts during training depends on the motion accuracy of the end effector, and the operational feeling improves with higher motion accuracies [28]. Therefore, the control goal of the force–position hybrid control strategy is to render the motion accuracy of the end effector as accurately as possible [29]. However, the cable is an elastomer. Measuring the elastic deformation of the cable is difficult and will affect the movement accuracy of the operation object [30]. Currently, most research results do not consider the problems caused by the deformation of the cable. A

few scholars have pointed out that the model of the cable is more complex and put forward the following problem: the elastic deformation of the cable in the astronaut microgravity training system will lead to lower motion accuracy of the end mechanism; however, no solution to this problem has been proposed [31,32]. In addition, the existing control strategy is very sensitive to motion disturbances, and the force control error fluctuates obviously, which limits further improvements with respect to the control accuracy [33].

In summary, the classical motion method and force balance method have problems such as low safety, high costs, and parameters of the operating object that cannot be set arbitrarily using the software. The virtual microgravity training method based on cable-driven technology that has emerged in recent years has solved these problems, but the control strategy used in this method has the following problem: The elastic deformation of the cable affects the accuracy of motion control. The above problems will directly affect the training experience of astronauts. Due to the above problems, this study designed a virtual microgravity training system for astronauts, and it is driven by parallel cables based on VR vision technology (hereinafter referred to as “VRCDVMTS”); moreover, we propose a new composite control strategy that effectively improves motion control accuracy by allocating cable tension and using a tension compliance control method to suppress the influence of cable deformation.

2. Working Principle of the Virtual Microgravity Training System

2.1. Movement Model of the Microgravity Environment Object

“The motion law of an object” in the microgravity environment refers to the motion mode of the inertial body (frictionless and microgravity) under the action of external forces. The motion law can be expressed as follows:

$$X_t = f_{ml}(F_h) \tag{1}$$

where X_t is the target position vector of the virtual object, F_h is the interaction force between an astronaut and the virtual object, and these exhibit the following:

$$\begin{aligned} X_t &= [X_{tx} \quad X_{ty} \quad X_{tz} \quad \theta_{tx} \quad \theta_{ty} \quad \theta_{tz}]^T, \\ F_h &= [F_{hx} \quad F_{hy} \quad F_{hz} \quad M_{hx} \quad M_{hy} \quad M_{hz}]^T \end{aligned}$$

This equation is derived from the force balance equation for objects in a microgravity environment:

$$\begin{cases} F_{hx} = m_0 \ddot{X}_{tx} \\ F_{hy} - m_0 g = m_0 \ddot{X}_{ty} \\ F_{hz} = m_0 \ddot{X}_{tz} \end{cases} \tag{2}$$

$$\begin{bmatrix} M_{hx} \\ M_{hy} \\ M_{hz} \end{bmatrix} + \begin{bmatrix} 0 & F_{hz} & -F_{hy} \\ -F_{hz} & 0 & F_{hx} \\ F_{hy} & -F_{hx} & 0 \end{bmatrix} C_0 = \begin{bmatrix} J_{0x} \ddot{\theta}_{tx} \\ J_{0y} \ddot{\theta}_{ty} \\ J_{0z} \ddot{\theta}_{tz} \end{bmatrix} \tag{3}$$

where C_0 is the position deviation of the astronaut operation center and the center of the virtual object, and it exhibits $C_0 = [C_{0x} \quad C_{0y} \quad C_{0z}]^T$; m_0 is the virtual object mass; J_{0x} , J_{0y} , and J_{0z} are the moments of inertia of the virtual object.

Using Equations (2) and (3) simultaneously, the two sides of the equation are integrated:

$$\begin{cases} V_t = \int_0^T J_0^{-1} (F_h + \begin{bmatrix} m_0 g_0 \\ NC_0 \end{bmatrix}) dt + V_0 \\ X_t = \int_0^T V_t dt + X_0 \end{cases} \tag{4}$$

where J_0 is the virtual object inertia vector; g_0 is the virtual environment gravity acceleration; V_t is the virtual object target velocity; V_0 is the initial velocity of the virtual object; X_0 is the initial position of the virtual object, and they exhibit the following:

$$J_0 = [m_0 \quad m_0 \quad m_0 \quad J_{0x} \quad J_{0y} \quad J_{0z}]^{\times}, V_t = [\dot{X}_{tx} \quad \dot{X}_{ty} \quad \dot{X}_{tz} \quad \dot{\theta}_{tx} \quad \dot{\theta}_{ty} \quad \dot{\theta}_{tz}]^T$$

$$g_0 = [g_{0x} \quad g_{0y} \quad g_{0z}]^T, N = \begin{bmatrix} 0 & F_{hz} & -F_{hy} \\ -F_{hz} & 0 & F_{hx} \\ F_{hy} & -F_{hx} & 0 \end{bmatrix}$$

The motion law of the virtual object (virtual inertia vector J_0) under the interaction force F_h of an astronaut is shown in Equation (4). In training, changing m_0 can change the mass of the virtual object, changing J_0 can change the inertia of the virtual object, and changing g_0 can alter the gravitational acceleration of the space environment. In this way, the motion law for handling objects with different masses and inertia can be realized in any microgravity environment. Therefore, Equation (4) can describe the motion control law of the end of the virtual training device under the action of interacting forces, and Equation (4) provides a theoretical basis for planning the trajectory of the virtual object.

2.2. Structural Principle of the Training System

The overall structural model is shown in Figure 1a. The system consists of the end effector (operation object), cables, cable drive units, and VR glasses. Cable drive units use the rod slider mechanism to drive the cable’s movement using the slider’s movement.

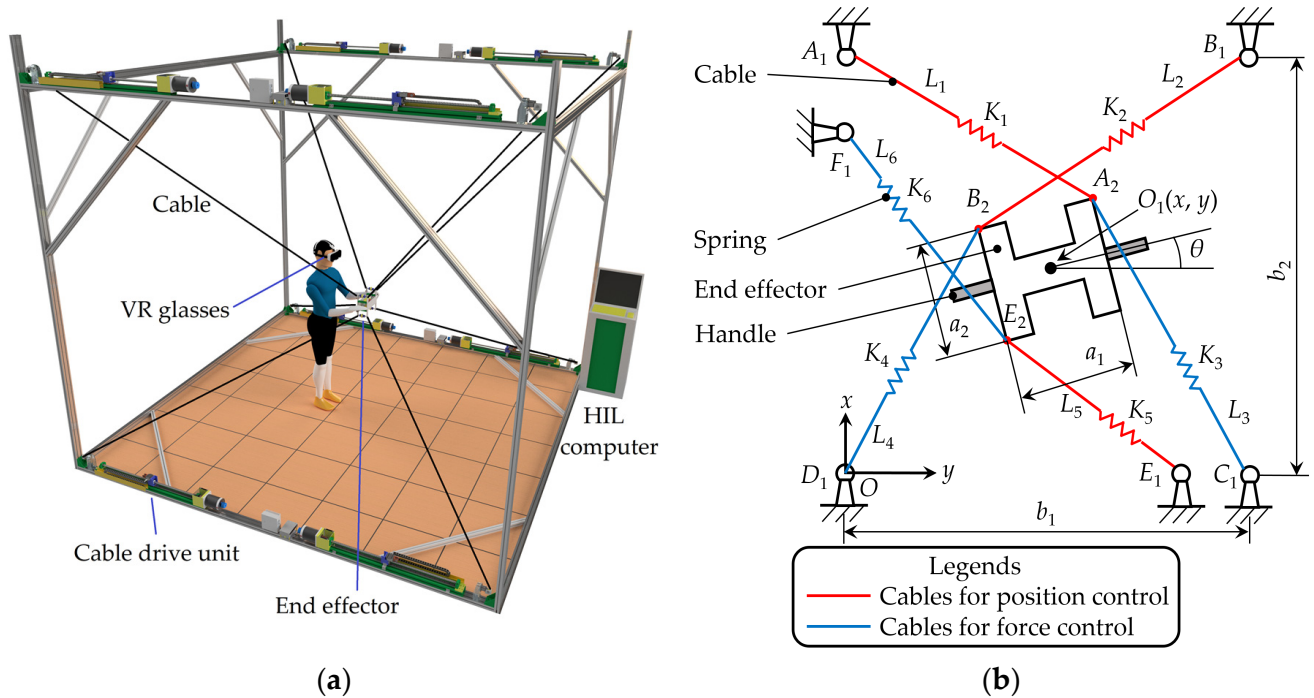


Figure 1. System structure: (a) overall structure; (b) the plane actuator of the training system.

VRCDVMTS’s working principle is to sample the interaction force between the astronaut and the virtual object (operation object), and it calculates the motion law of the virtual object using Equation (4) as the input condition of the system. The movement of cables is controlled via a control strategy. The end effector of the training device conforms to the motion law of the virtual object in the microgravity environment.

2.3. Control Principle of the Training System

2.3.1. The Basic Principle

VRCDVMTS has two groups of cables, namely position-controlling (hereinafter “LP”) and tension-controlling (hereinafter “LF”) cables. The function of LP is to control the position and pose of the end effector. Due to the inability to directly control the posture of the end effector, the posture of the end effector is indirectly controlled by controlling the displacement of LP [34]. LF has two functions. The first function is to control the tension of LP; thus, the shape variables of LP remain unchanged and improve the control accuracy of the end effector. The second function is to increase the number of drivers so that it is greater than the number of degrees of freedom. Because the cable cannot provide pressure [35], a greater number of drives is needed to maintain a certain amount of tension [36]. That is, the system is a redundant drive system [37].

A plane mechanism, which is shown in Figure 1b, is used as an example to analyze the principle of the training system. The end effector of the actuator is the operation object of the astronaut. The red cables comprise LP (L_1 , L_2 , and L_5); the blue cables comprise LF (L_3 , L_4 , and L_6). The drive ends of the cables ($A_1 \sim E_1$) are distributed at the edge of the actuator, and the other cable ends and the three vertices of the end effector (A_2 , B_2 , and E_2) can be linked together. The cables drive the end effector’s motion in order to control the position and pose of the end actuator. Moreover, this achieves the plane’s 3 DOF motion ($X = [x \ y \ \theta]^T$), namely x - and y -direction displacement and rotation around the z -axis.

When the cable’s mass is ignored, its elastic deformation is as follows:

$$\Delta L = \frac{4F \cdot L_c}{E \cdot \pi d^2} = K_c F \quad (5)$$

where F is the cable tension, L_c is the original length when the cable is free from tension, E is the cable’s elastic modulus, d is the diameter of the cable, and K_c is the cable elasticity coefficient.

From Equation (5), for a known cable, E , L_c , and d remain constant, and its deformation is related to its original length (cable length at 0 tension) and tension [38]. Therefore, during astronaut training, the tension of red cables (LP) is controlled so that it remains unchanged, as shown in Figure 1b. Cable drive units use the screw slide module to replace the winding mechanism, which ensures that the original length of the cable is constant. The above methods ensure that the elastic deformation of cables remains unchanged, effectively improving the control accuracy of the end effector.

The reason why the number of cables for LF is three is that for the 3 DOF system, at least three adjustable forces are required to balance the system. The tension of the LP is constant and not adjustable; thus, LF requires at least three cables to provide three adjustable forces. To simplify the structure, the minimum number of cables is used here.

2.3.2. The Compliance Control Method for Loading Tension

Aiming at the difficulty of improving the control accuracy and stability of the classic force servo system, a compliance control method is used to introduce improvements to the tension control method of LF.

As shown in Figure 2, the spring is arranged in a series with the cable (LF) to control the tension, and cable tension is controlled by controlling the elongation of the spring to transform the force control into displacement control. This not only avoids low robustness and low precision problems with respect to the existing force control system but can also obtain the impedance control effect. The method gives full play to the characteristics (maturity and easily achieved high control accuracy) of servo position control technologies. In Figure 2, F_t is the target tension of the cable, and L_t is the displacement of the cable without considering spring elasticity.

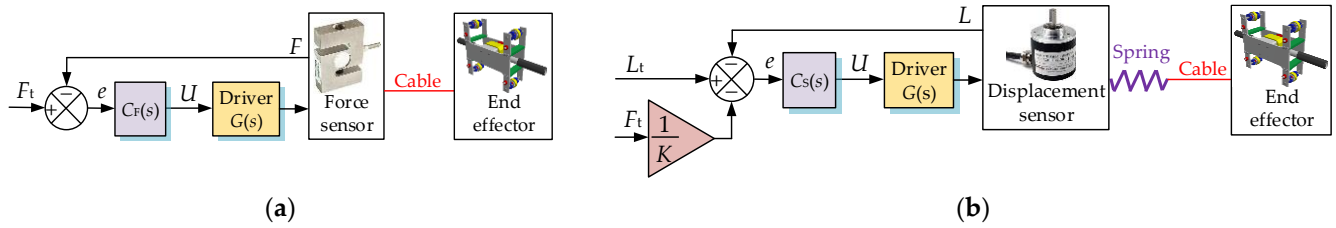


Figure 2. Control methods of cable tension: (a) typical force control method; (b) improved force control method.

2.3.3. The New Composite Control Strategy

The control block diagram of VRCDVMTS is shown in Figure 3, and the functions of each part are as follows:

1. The microgravity environment model

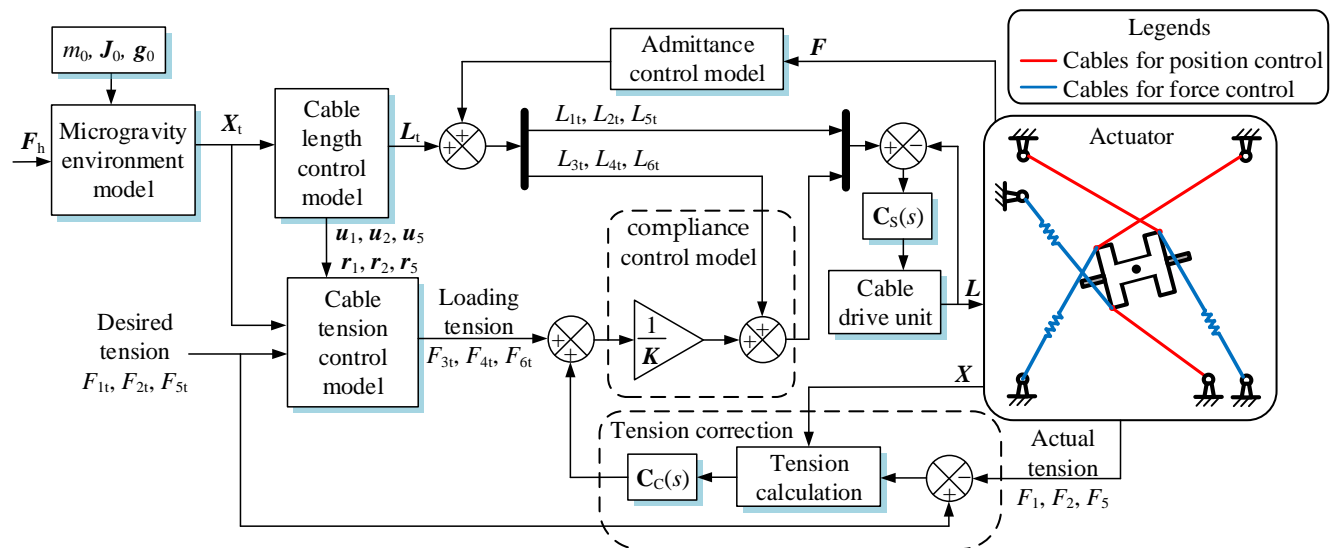


Figure 3. The overall control block diagram of the new composite control strategy.

A microgravity environment model is established using Equation (4) to generate the target position (X_t) of the virtual object in a microgravity environment (g_0) under the interaction (F_h) of an astronaut. Equation (4) provides a theoretical basis for planning the trajectory of the virtual object.

2. Cable length control model

The function of this model is to solve the target length (L_t) of six cables using the inverse kinematics formulas of the actuator based on the target position (X_t) of the virtual object.

3. Cable tension control model

The loading tension of LF (F_{3t} , F_{4t} , and F_{6t}) is calculated using the inverse dynamic formulas of the actuator. By controlling the loading tension of LF, the tension of LP is indirectly controlled. At the same time, the desired tension of LP (F_{1t} , F_{2t} , and F_{5t}) is optimized based on the system’s workspace, enabling the system to achieve more complex training tasks.

4. The compliance control model for loading tension

The model uses springs to generate tension in LF. The loading tension (F_{3t} , F_{4t} , and F_{6t}) is converted into spring elongation, and this compensates for the original calculated cable length. The cable’s tension is controlled by controlling the cable’s length (displacement).

5. Tension correction model

The actual tension of LP ($F_1, F_2,$ and F_5) is sampled, and a tension correction model is used to compensate for the loading tension of LF. Thus, the tension error of LP is reduced, the elongation of cables is more stable, and the control accuracy of the end effector is further improved.

6. Cable drive units

The servo position system is used to control the displacement of all cables. The admittance control module is the safe part of the system. Its purpose is to ensure that the cable’s tension is within the safe range. Moreover, the admittance control module uses “spring-mass-damping” structure.

3. System Control Model

3.1. Cable Length Control Model

As shown in Figure 1b, the global coordinate origin of the actuator is O , and the local coordinate origin of the end effector is O_1 . The actuator’s kinematic equation is as follows:

$$\begin{cases} l_i = c_i - (d_i + {}^O R_{O_1} r_i), & i = 1, \dots, 6 \\ u_i = l_i / \|l_i\|, & i = 1, \dots, 6 \end{cases} \tag{6}$$

where u_i represents the directional vector of cables; r_i represents the direction vector (the local coordinate system’s origin O_1 to the end point of the cable); l_i represents the direction vector of the cable; c_i represents the vector of the cable’s guide wheel in the global coordinate system; d_i represents the vector of the local coordinate origin, O_1 , in the global coordinate system; r_i represents the vector of the endpoint of the cable in the local coordinate system; ${}^O R_{O_1}$ represents the rotation matrix from the local coordinate system to the global coordinate system, and it exhibits the following:

$${}^O R_{O_1} = \begin{bmatrix} \cos \theta & \sin \theta \\ -\sin \theta & \cos \theta \end{bmatrix} \tag{7}$$

The cable’s rotation angle is as follows:

$$\theta_i = \arccos \frac{l_i \cdot x_0}{\|l_i\| \|x_0\|}, i = 1, \dots, 6 \tag{8}$$

where x_0 denotes the x -direction vector of the global coordinate system.

3.2. Cable Loading Tension Control Model

3.2.1. Dynamic Model of the Actuator

The mass of the cables can be ignored, and the elasticity of the cables cannot be ignored. The end effector’s mass is large, and there may be substantial speed and acceleration during movements; thus, the mass and inertia of the end effector should not be ignored [39]. The cable’s elastic equation for the actuator is as follows:

$$L = L_c + KF \tag{9}$$

where L is the actual length of the cable; L_c is the length of the cable when it is free from tension; K is the comprehensive elasticity coefficient of the cables and springs; F is the actual tension of the cables, and it exhibits the following:

$$K = \begin{bmatrix} K_1 & & \\ & \ddots & \\ & & K_6 \end{bmatrix}, F = [F_1 \quad F_2 \quad \dots \quad F_6]^T$$

The dynamic equation for the actuator is as follows:

$$J\mathbf{F} + \mathbf{G} + \mathbf{F}_{h2} = M\ddot{\mathbf{X}} + W\dot{\mathbf{X}} \tag{10}$$

where \mathbf{F}_{h2} is the planar interaction force vector, \mathbf{G} is the gravity vector, \mathbf{X} is the position vector of the end effector in the global coordinate system, and the following equations are exhibited:

$$J = \begin{bmatrix} \mathbf{u}_1 & \mathbf{u}_2 & \cdots & \mathbf{u}_6 \\ \mathbf{r}_1 \times \mathbf{u}_1 & \mathbf{r}_2 \times \mathbf{u}_2 & \cdots & \mathbf{r}_6 \times \mathbf{u}_6 \end{bmatrix}, \mathbf{F}_{h2} = [F_{hx} \quad F_{hy} \quad M_{hz}]^T$$

$$\mathbf{G} = [0 \quad -mg \quad mgC_x]^T, \mathbf{X} = [x \quad y \quad \theta]^T$$

$$M = \begin{bmatrix} m \begin{bmatrix} 1 & 0 \\ 0 & 1 \end{bmatrix} & -m \begin{bmatrix} C_y \\ C_x \end{bmatrix} \\ m \begin{bmatrix} C_y & C_x \end{bmatrix} & J_z \end{bmatrix}, W = \begin{bmatrix} 0 & -m\dot{\theta} \begin{bmatrix} C_y \\ C_x \end{bmatrix} \\ m\dot{\theta} \begin{bmatrix} C_y & C_x \end{bmatrix} & -J_z\dot{\theta} \end{bmatrix}$$

where m is the end effector’s mass, J_z represents the inertia of the end actuator along the z -axis in the local coordinate system, and $\mathbf{C} = [C_x \quad C_y]^T$ represents the local coordinate system’s origin position vector, $O1$, up to the center of mass of the end effector.

3.2.2. Load the Tension Model

In order to accurately control the motion of the end effector, it is necessary to simultaneously control the displacement and tension of LP. The displacement is controlled directly; thus, tension is controlled indirectly. By controlling the loading tension of LF (F_{3t}, F_{4t}, F_{6t}), the tension of LP (F_{1t}, F_{2t} , and F_{5t}) is indirectly controlled.

From the kinetic model of Equation (10), the loading tension of cables is as follows:

$$\begin{bmatrix} F_{3t} \\ F_{4t} \\ F_{6t} \end{bmatrix} = P_2^{-1} \left(M\ddot{\mathbf{X}} + W\dot{\mathbf{X}} - \mathbf{F}_{h2} - \mathbf{G} - P_1 \begin{bmatrix} F_{1t} \\ F_{2t} \\ F_{5t} \end{bmatrix} \right) \tag{11}$$

where

$$P_1 = \begin{bmatrix} \mathbf{u}_1 & \mathbf{u}_2 & \mathbf{u}_5 \\ \mathbf{r}_1 \times \mathbf{u}_1 & \mathbf{r}_2 \times \mathbf{u}_2 & \mathbf{r}_5 \times \mathbf{u}_5 \end{bmatrix} = \begin{bmatrix} \cos \theta_1 & \sin \theta_1 & h_1 \sin(-\theta_1 + h_2 + \theta) \\ \cos \theta_2 & \sin \theta_2 & -h_1 \sin(\pi + \theta_2 + h_2 - \theta) \\ \cos \theta_5 & \sin \theta_5 & h_1 \sin(\pi - \theta_5 + h_2 + \theta) \end{bmatrix}^T$$

$$P_2 = \begin{bmatrix} \mathbf{u}_3 & \mathbf{u}_4 & \mathbf{u}_6 \\ \mathbf{r}_3 \times \mathbf{u}_3 & \mathbf{r}_4 \times \mathbf{u}_4 & \mathbf{r}_6 \times \mathbf{u}_6 \end{bmatrix} = \begin{bmatrix} \cos \theta_3 & \sin \theta_3 & -h_1 \sin(\theta_3 - h_2 - \theta) \\ \cos \theta_4 & \sin \theta_4 & h_1 \sin(\pi - \theta_4 - h_2 + \theta) \\ \cos \theta_6 & \sin \theta_6 & -h_1 \sin(\pi + \theta_6 - h_2 - \theta) \end{bmatrix}^T$$

$$h_1 = \frac{\sqrt{a_1^2 + a_2^2}}{2}, h_2 = \arctan \frac{a_2}{a_1}$$

The cable tension correction module is the closed-loop tension controller of LP, and it is designed to further reduce the difference between the actual tension (F_1, F_2, F_5) and the desired tension (F_{1t}, F_{2t}, F_{5t}). This difference is the slight deviation between the structural parameters of the actual system and the theoretical parameters. $C_C(s)$ is the controller of the module, and the tension solution calculation link includes the inverse kinematic and the inverse dynamic formulas of the actuator. Let the output value of the tension solution link be “ F_c ”; then, we obtain the following:

$$\mathbf{F}_c = \begin{bmatrix} F_{c3} \\ F_{c4} \\ F_{c6} \end{bmatrix} = -P_2^{-1} P_1 \begin{bmatrix} F_{1t} - F_1 \\ F_{2t} - F_2 \\ F_{5t} - F_5 \end{bmatrix} \tag{12}$$

3.3. Cable Desired Tension Control Model

3.3.1. The Calculation Principle of the Desired Tension

The new composite control strategy proposed in this article effectively improves the motion control accuracy of the end effector, but the desired tension value of cables will affect the working space of the system. The workspace of the system refers to the feasible working area of the end effector. The larger the working space of the system, the larger the range of motion, and more complex training tasks can be performed by astronauts. It is, therefore, necessary to calculate the desired tension of LP when the system’s workspace is maximized.

3.3.2. System Workspace Model

In the feasible working area, the system needs to meet two conditions: first, the cables and the end effector cannot interfere with one another; second, the tension of all cables is within the allowable range [40].

1. Interference conditions

When astronauts conduct virtual operation training, they sometimes need to carry out torsion operations. When the rotation angle of the end effector, θ , is too large, the cable will collide with the end surface of the end effector. The relationship between the cable and the end effector’s boundary vector is shown in Figure 4. Interference is determined based on whether the boundary vector between the cable and the end effector is parallel [41].

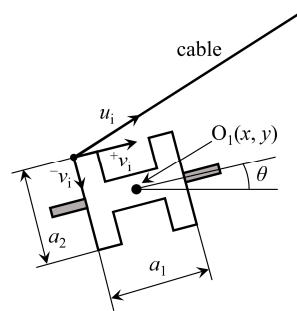


Figure 4. Cable and end effector boundary vector.

The critical condition for interference between the cable and the end effector is as follows:

$$u_i = +v_i \text{ or } u_i = -v_i \quad (i = 1, \dots, 6) \tag{13}$$

Substituting the structural parameters of the actuator into the above equation, the condition for no interference is as follows:

$$\arccos \frac{u_i \cdot x_0}{|u_i| |x_0|} > \arccos \frac{+v_i \cdot x_0}{|+v_i| |x_0|} \text{ and } \arccos \frac{u_i \cdot x_0}{|u_i| |x_0|} < \arccos \frac{-v_i \cdot x_0}{|-v_i| |x_0|}, \quad i = 1, \dots, 6 \tag{14}$$

2. Range of allowable tension

Considering the safety of the system and the driving ability of drive units, the cable’s tension has an upper limit. If the cable’s tension is too low, the cable will shake and affect the stability of the cable drive system; due to this, the cable’s tension has a lower limit. The upper limit of the cable tension is set to be F_{\max} , and the lower limit of the cable tension is F_{\min} . The allowable tension range of the cable is as follows:

$$F = \{F | F_{\min} < F_i < F_{\max}, \quad i = 1, \dots, 6\} \tag{15}$$

3. Workspace solution

The basic steps for solving the system’s workspace using the point-by-point comparison method are shown in Figure 5. Firstly, the motion region of the end effector is discretized

into several points. Then, substituting the desired tension of LP into Equation (11), the loading tension of LF can be obtained. If the obtained loading tension is within the allowable tension range and meets the non-interference condition, then the current working point is within the feasible working area; otherwise, the current working point is not within the feasible working area. Finally, whether each point meets the motion conditions in a sequence is determined, and all points that meet the conditions are combined to form the feasible working range of the system.

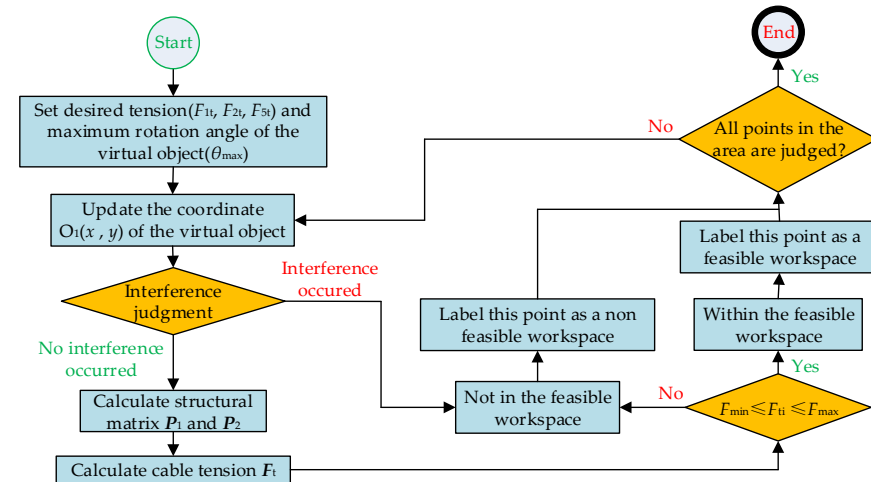


Figure 5. The feasible workspace’s algorithm flowchart.

Figure 6 shows a feasible workspace for different desired tension and turn angles. The actuator’s structural parameters are shown in Table 1, and the cable’s tension value range is set to $F_{max} = 150\text{ N}$ and $F_{min} = 10\text{ N}$.

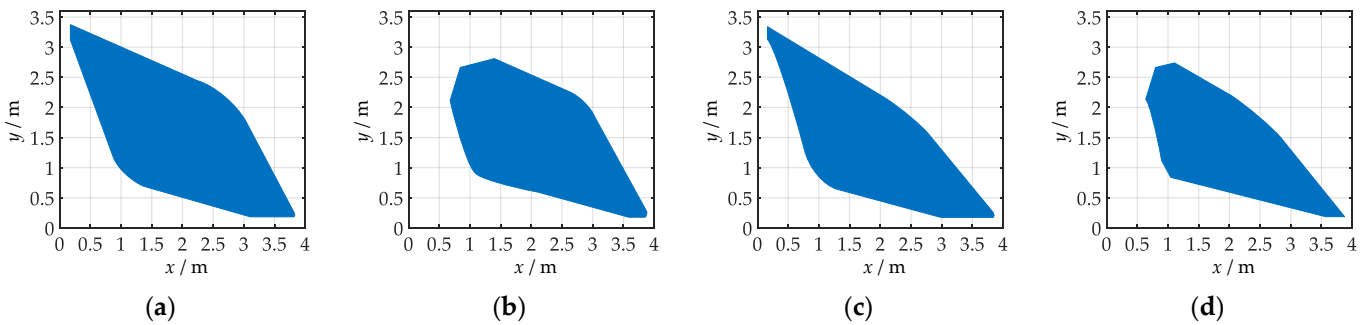


Figure 6. System workspace: (a) $F_{1t} = 60\text{ N}$, $F_{2t} = 60\text{ N}$, $F_{5t} = 50\text{ N}$, and $\theta = 0^\circ$; (b) $F_{1t} = 60\text{ N}$, $F_{2t} = 60\text{ N}$, $F_{5t} = 50\text{ N}$, and $\theta = 15^\circ$; (c) $F_{1t} = 40\text{ N}$, $F_{2t} = 40\text{ N}$, $F_{5t} = 70\text{ N}$, and $\theta = 0^\circ$; (d) $F_{1t} = 40\text{ N}$, $F_{2t} = 40\text{ N}$, $F_{5t} = 70\text{ N}$, and $\theta = 15^\circ$.

Table 1. The actuator’s structural parameters.

Parameter	Symbol	Unit	Value
Actual object mass	m	kg	2.1
Actual object inertia	J_z	$\text{kg}\cdot\text{m}^2$	0.035
Combined elastic coefficient of No. 3 cable and spring	K_3	N/m	3100
Combined elastic coefficient of No. 4 cable and spring	K_4	N/m	3100
Combined elastic coefficient of No. 6 cable and spring	K_6	N/m	3200

According to Figure 6, the desired tension of LP affects the system’s working space, and the larger the corner of the virtual object, the smaller the working space.

3.3.3. Desired Cable Tension Analysis

The actuator’s structural parameters are shown in Table 1, and the cable’s tension value range is set to $F_{\max} = 150$ N and $F_{\min} = 10$ N; moreover, the maximum rotation angle of the end actuator is $\theta_{\max} = 15^\circ$. With the exception of F_{5t} using tension values from 30 to 80 N, the area of the working space corresponding to different expected tension values is shown in Figure 7.

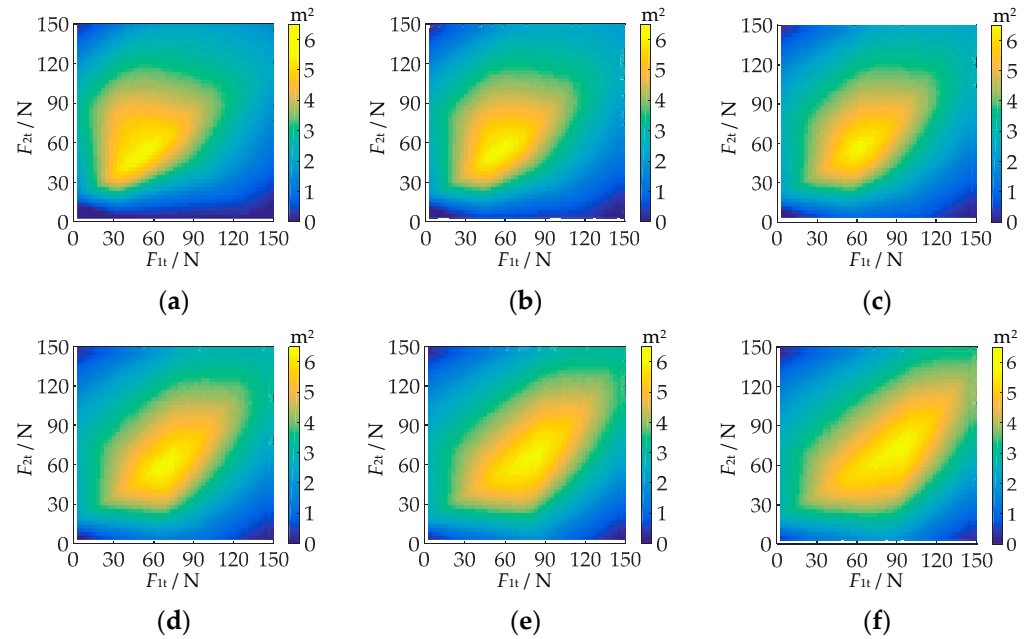


Figure 7. Area comparison in the workspace: (a) $F_{5t} = 30$ N; (b) $F_{5t} = 40$ N; (c) $F_{5t} = 50$ N; (d) $F_{5t} = 60$ N; (e) $F_{5t} = 70$ N; (f) $F_{5t} = 80$ N.

Figure 7 shows the desired tension of LP at given cable drive unit structural parameters: When the system’s working space is maximized, the parameters are $F_{1t} = 63$ N, $F_{2t} = 57$ N, and $F_{5t} = 50$ N. The corresponding workspace is shown in Figure 8.

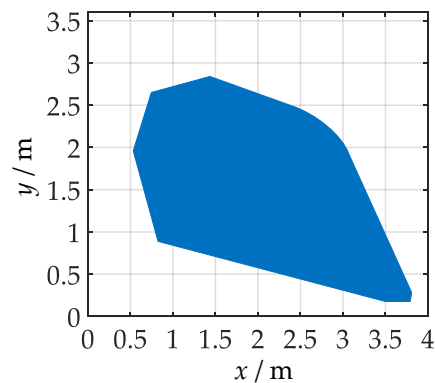


Figure 8. Maximum working space of the system.

4. Experimental Results and Discussion

4.1. Experimental Environment

The control system uses the HIL semi-physical simulation system, and the system’s control strategy runs in the semi-physical simulation host. The overall control structure is shown in Figure 9a; the actual experimental equipment is shown in Figure 9b. The system’s structural hardware parameters are shown in Table 1.

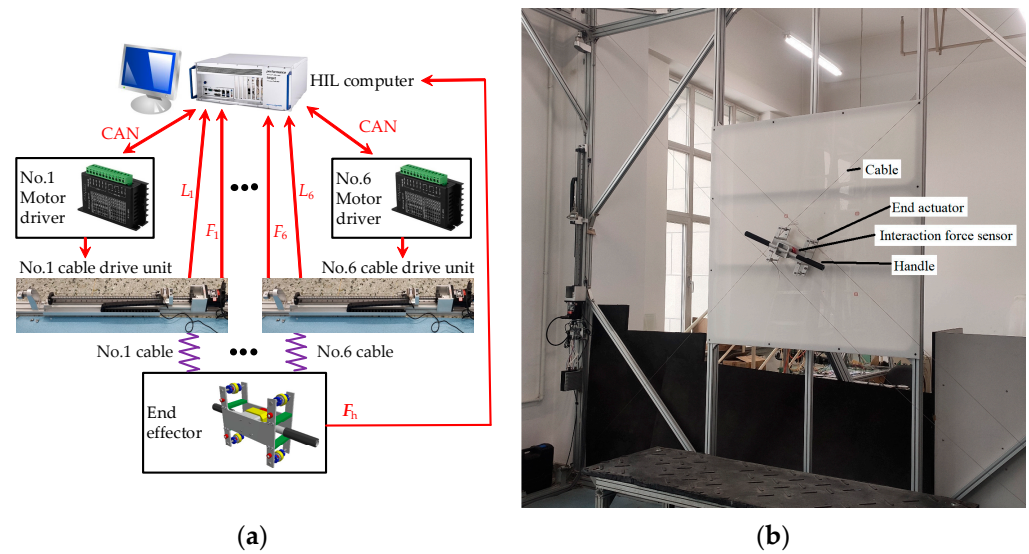


Figure 9. Experimental system: (a) overall control structure of the experimental system; (b) physical objects of the experimental equipment.

4.2. Tension Control Experiments

4.2.1. Experimental Results

To evaluate the control effect of the new composite control strategy on the tension of LP and the tension control method based on compliance control relative to the tension of LF, four groups of comparison experiments were carried out. The end effector moves in the x direction. In each group of experiments, the motion speed of the end effector exhibits a sinusoidal curve with different amplitudes and frequencies, and the velocity parameters are shown in Table 2. The controller’s parameters are shown in Table 3. The desired tension of LP is $F_{1t} = 63$ N, $F_{2t} = 57$ N, and $F_{5t} = 50$ N. Figure 10 shows tension errors of LP and LF. Figure 11 shows Maximum tension errors of cables.

Table 2. Velocity parameters of the end effector.

Experimental Grouping	Velocity Amplitude A_V /(m/s)	Velocity Frequency f_V /(Hz)
Group 1	0	-
Group 2	0.5	0.2
Group 3	1	0.2
Group 4	1	0.5

Table 3. Controller parameters.

Controller	Type	Variable K_P	Variable K_I	Variable K_D
$C_S(s)$	PD controller	7500	-	1600
$C_F(s)$	PID controller	1	43	0.07
$C_C(s)$	PI controller	9	105	-

4.2.2. Discussion of Tension Control Experiments

1. During the end effector’s movement, the greater the amplitude of the velocity change, the greater the tension error of each cable, while the velocity change frequency has little effect on the tension error of each cable. This suggests that the speed of the end effector is one of the sources of disturbance relative to the tension control system.
2. When the end effector is stationary, the maximum tension error of each cable is within 0.09 N, fluctuation exhibits good stability, and the tensions of LP at this time have the best accuracy.

3. The speed of the astronaut operating the object is usually below 1 m/s. When the end effector is in the worst working conditions ($A_V = 1$ m/s and $f_V = 0.5$ Hz), the maximum tension error of LP is 0.59 N, 0.62 N, and 0.53 N.
4. The new composite control strategy is effective. The tension control model, the tension control method based on compliance control, and the tension correction model are correct, achieving the purpose of controlling the tensions of the LP constant.

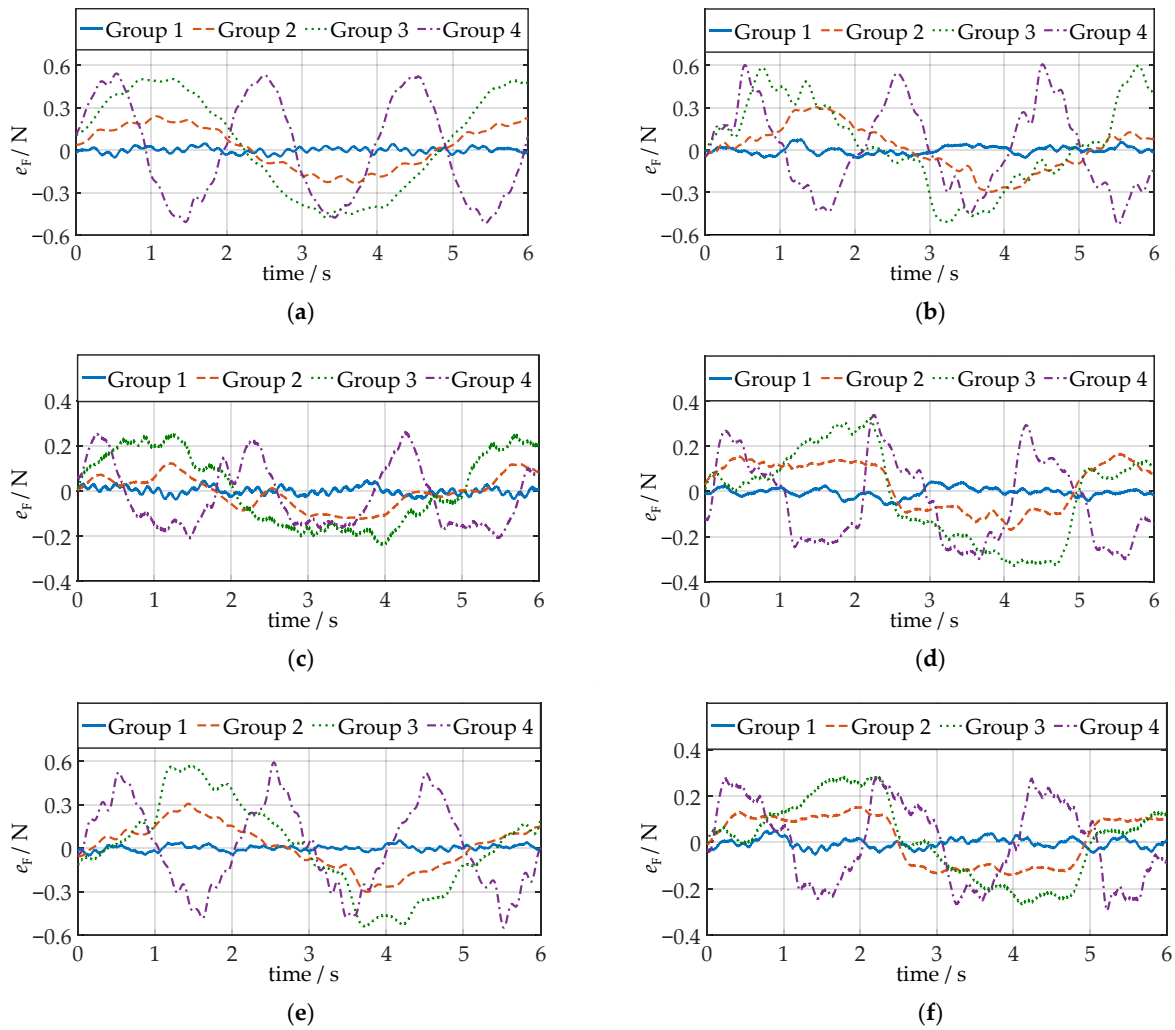


Figure 10. Tension errors: (a) No. 1 cable of LP; (b) No. 2 cable of LP; (c) No. 3 cable of LF; (d) No. 4 cable of LF; (e) No. 5 cable of LP; (f) No. 6 cable of LF.

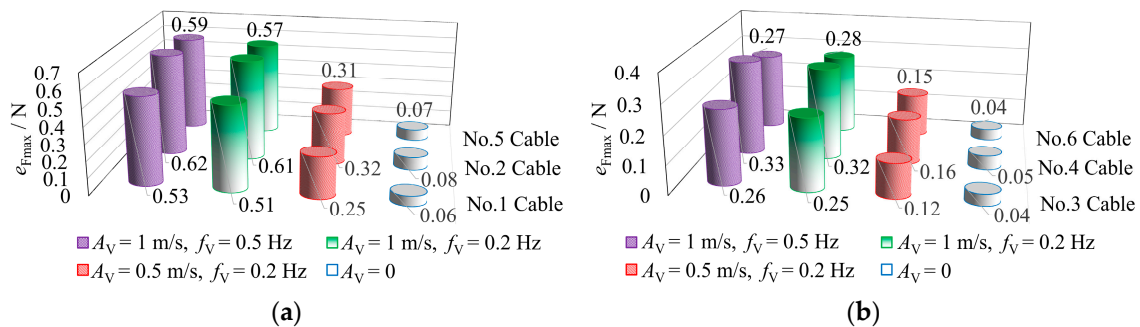


Figure 11. Maximum tension errors: (a) comparison of the maximum tension errors of LP; (b) comparison of the maximum tension errors of LF.

4.3. Motion Control Experiments

4.3.1. Experimental Results

To evaluate the effect of the new composite control strategy on the improvement of end effector control performance, four groups of comparative experiments were performed. In each group of experiments, the desired tension of LP exhibits sinusoidal curves with different amplitudes and frequencies. The median values of the sine curves are $F_{1t} = 63$ N, $F_{2t} = 57$ N, and $F_{5t} = 50$ N. The tension's amplitude and frequency parameters are shown in Table 4. The controller's parameters are shown in Table 2. Figure 12 shows the velocity errors of the end effector and the comparison of maximum velocity errors. The x direction is the horizontal direction, the y direction is the vertical direction, $e_{V_{max}}$ is the maximum value of velocity errors, and $e_{\omega_{max}}$ is the maximum value of angular velocity errors.

Table 4. Desired tension parameters of LP.

Experimental Grouping	Force Amplitude A_F /(N)	Force Frequency f_F /(Hz)
Group 1	0	-
Group 2	5	1
Group 3	10	1
Group 4	10	2

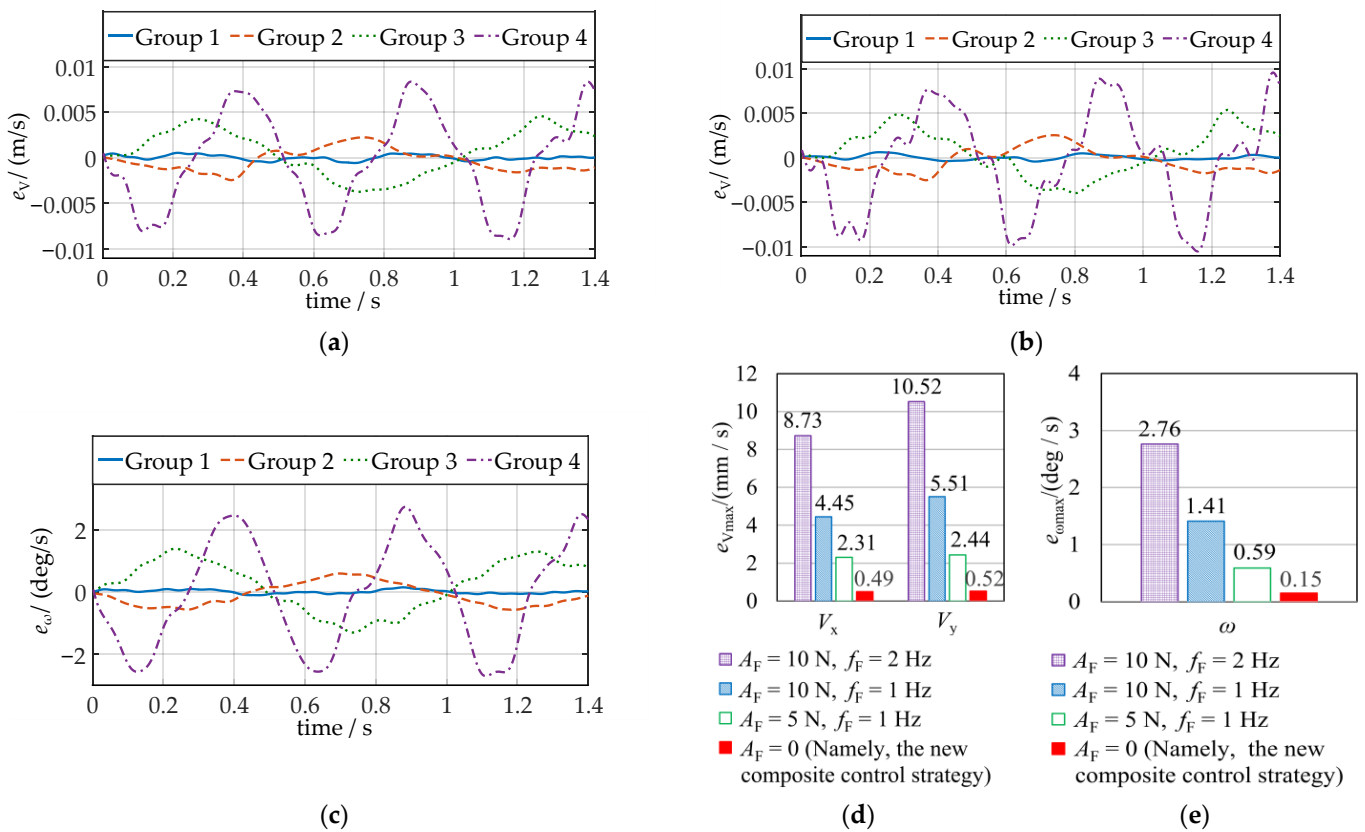


Figure 12. End effector velocity errors and comparison of velocity errors: (a) velocity errors in the x direction; (b) velocity errors in the y direction; (c) angular velocity errors; (d) comparison of maximum velocity errors; (e) comparison of maximum angular velocity errors.

For maximum velocity error elimination, 94.4% (x direction), 95.1% (y direction), and 94.6% (rotation direction) were used. The maximum velocity error elimination rate η_V can be expressed as follows:

$$\eta_V = \frac{|e_{V_a}|_{\max} - |e_{V_b}|_{\max}}{|e_{V_a}|_{\max}} \times 100\% \quad (16)$$

where e_{V_a} is the velocity error when the new composite control strategy is not used ($A_F = 10$ N and $f_F = 2$ Hz); e_{V_b} is the velocity error when using the new composite control strategy ($A_F = 0$).

4.3.2. Discussion of Tension Control Experiments

1. The more obvious the change in the tension of LP (greater A_F or f_F), the greater the velocity error of the end effector. Therefore, the higher the tension control accuracy of the cable, the higher the motion accuracy of the end effector. Moreover, a force control method with high accuracy and good stability is required.
2. Compared to using the new composite control strategy and not using the new composite control strategy, the velocity error is significantly reduced. The maximum velocity error elimination rates are 94.4% (x direction), 95.4% (y direction), and 94.6% (rotation direction);
3. The new composite control strategy is effective. The cable length allocation model, the tension control method based on compliance control, and the tension control model are correct. The purpose of improving the control accuracy of a virtual object's position is achieved.

4.4. VRCDVMTS's Comprehensive Experiments

4.4.1. Experimental Results

To evaluate the performance of VRCDVMTS during astronaut training, the trajectory of the virtual object was constructed, as shown in Figure 13. The steps for the astronaut to operate the virtual object are as follows:

1. When the virtual object is at point A in Figure 13, the initial velocity and initial displacement are both 0. The astronaut pushes the virtual object in the direction of x and stops the virtual object at point B. At this stage, the object experiences acceleration, uniform speed, and braking in the horizontal direction, simulating the astronaut's action of pushing the object in the horizontal direction.
2. The astronaut pushes the virtual object in the opposite direction of y and stops the virtual object at point C. At this stage, the object experiences acceleration, uniform speed, and braking in the vertical direction, simulating the astronaut's action of pushing the object along the vertical direction.
3. The astronaut rotates the virtual object counterclockwise. As shown in Figure 13, the virtual object rotates θ around the z -axis at point C. At this stage, the object experiences acceleration, uniform speed, and braking in the rotational direction, simulating the astronaut's action of rotating the object around the z -axis.

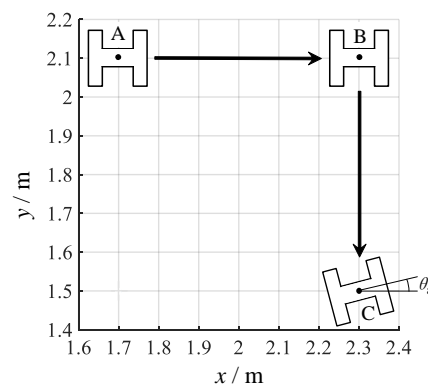


Figure 13. The trajectory of the virtual object's movement.

During the experiment, the astronaut operated the object according to the motion trajectory of the object shown in Figure 13. Two groups of experiments were conducted, and the virtual environment parameters of each experiment are shown in Table 5. These two groups of experiments show the performance of the system under different virtual mass and inertia parameters. The controller’s parameters are shown in Table 2; the astronaut’s interaction force and interaction moment curves are shown in Figure 14; the tension errors of LP are shown in Figure 15; the desired velocities and velocity errors of the end effector are shown in Figure 16.

Table 5. Virtual environment parameters.

Experimental Grouping	Virtual Mass m_0 /(kg)	Virtual Rotational Inertia J_{0z} /(kg·m ²)	Virtual Gravity g_0 /(m/s ²)
Group 1	20	1	0
Group 2	80	4	0

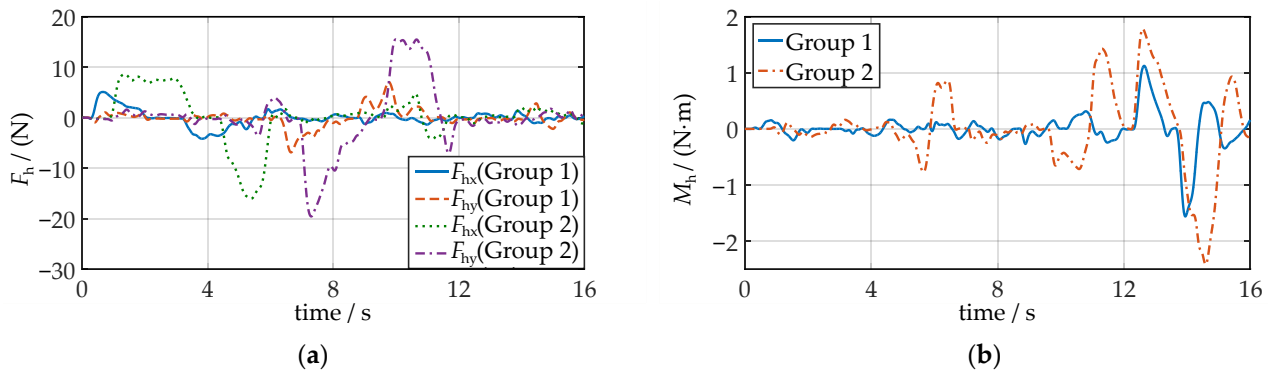


Figure 14. The interaction force and interaction moment curve. (a) Interaction force; (b) interaction moment.

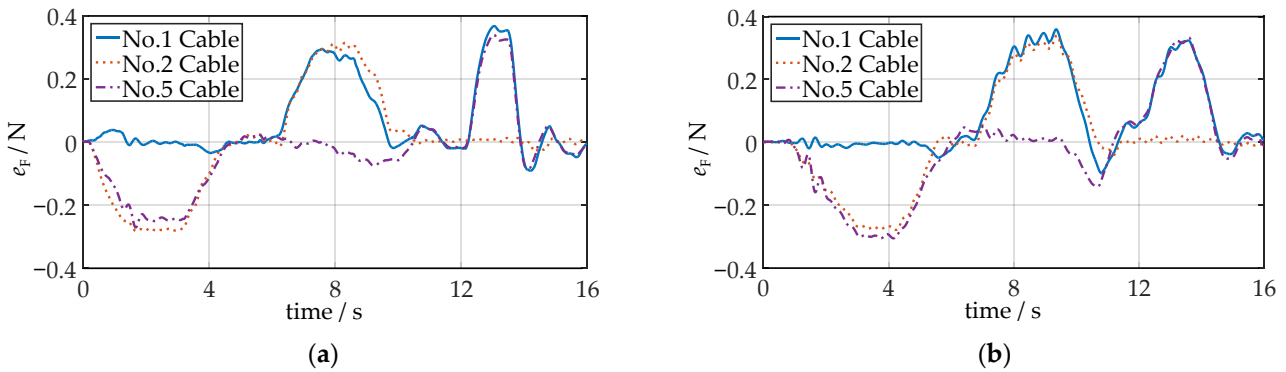


Figure 15. Tension errors of LP. (a) Experimental tension errors in Group 1; (b) experimental tension errors in Group 2.

The maximum tension errors of LP (Table 6) and the maximum end effector velocity errors (Table 7) are obtained from Figures 15 and 16.

Table 6. Maximum tension errors of LP.

Experimental Grouping	Maximum Tension Errors e_{Fmax} /(N)		
	No. 1 Cable	No. 2 Cable	No. 5 Cable
Group 1	0.37	0.32	0.34
Group 2	0.36	0.34	0.33

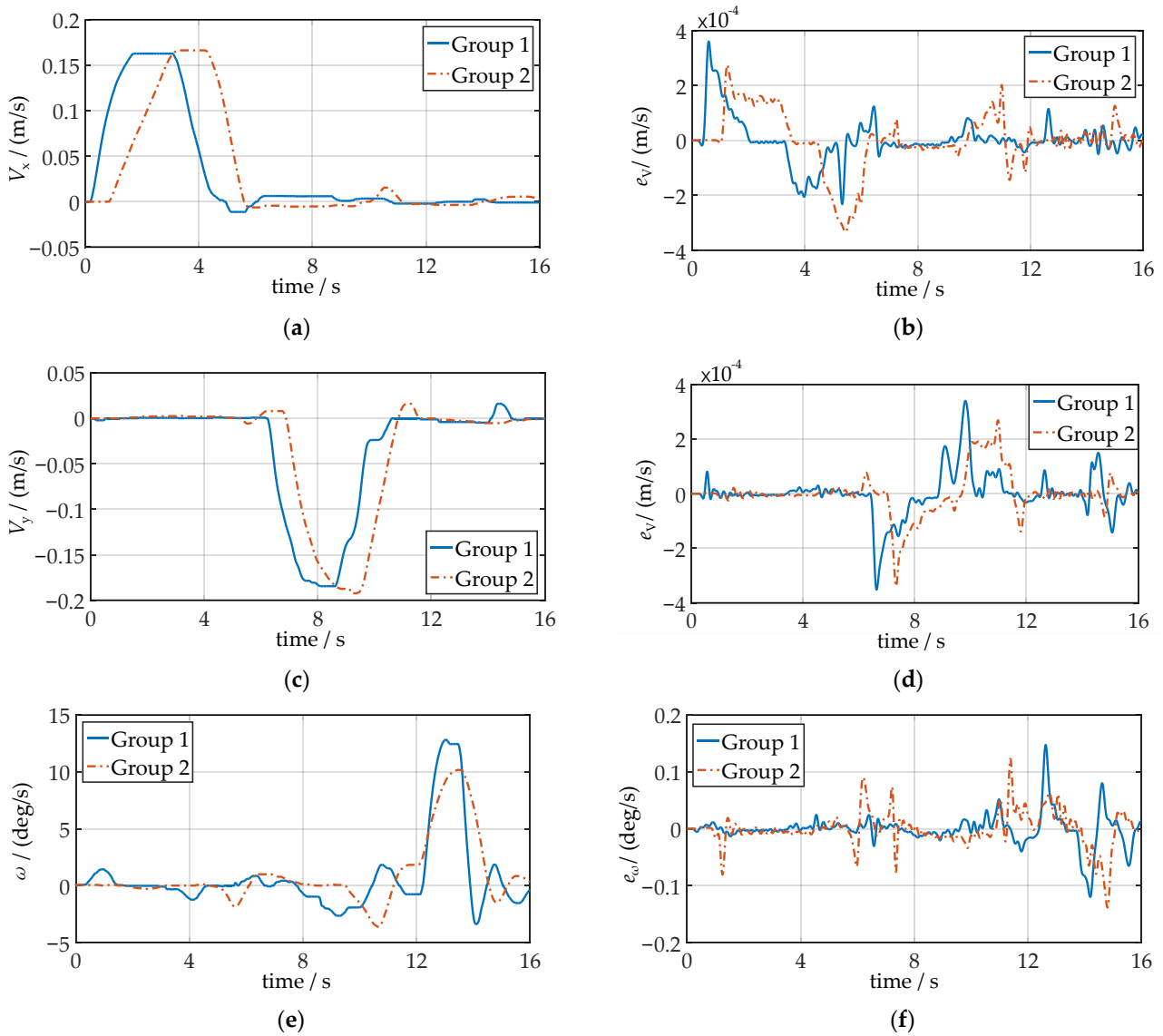


Figure 16. Desired velocities and velocity errors. (a) Desired velocities in the x direction of the end effector; (b) velocity errors in the x direction of the end effector; (c) desired velocities in the y direction of the end effector; (d) velocity errors in the y direction of the end effector; (e) desired velocities in the rotational direction of the end effector; (f) velocity errors in the rotational direction of the end effector.

Table 7. Maximum velocity errors of the end effector.

Experimental Grouping	Maximum Velocity Errors $e_{V_{max}}/(mm/s)$		Maximum Angular Velocity Errors $e_{\omega_{max}}/(deg/s)$
	x Direction	y Direction	
Group 1	0.36	0.35	0.15
Group 2	0.34	0.35	0.14

4.4.2. Discussion of the Comprehensive Experiment of VRCDVMTS

1. The virtual object’s parameters (virtual mass and virtual inertia) were changed, and no significant change was observed with respect to cable tension errors and the end effector’s velocity errors. This shows that the system’s control accuracy was not substantially affected by the change in the virtual object’s parameters, and by changing the virtual object’s parameters, the system could adapt to many different training items.

-
2. In the actual training experiment with the astronaut, the maximum tension errors of each cable did not exceed 0.37 N, and the new composite control was effective. The maximum velocity errors of the end effector did not exceed 0.36 mm/s, the maximum angular velocity errors did not exceed 0.15°/s, and high-precision motion control was realized throughout the entire process.

5. Conclusions

The VRCDVMTS system designed in this article can achieve object movement training for astronauts in simulated virtual gravity environments on the ground. Aiming at the problem where the elastic deformation of cables reduces the movement accuracy of the operation object and affects the astronaut feelings during operations, we designed a new composite control strategy that effectively improved the control accuracy of the working object. In addition, we calculated the system's workspace and set the desired tension of some cables according to the principle of workspace maximization to achieve more complex virtual microgravity training tasks.

Finally, the tension control model, cable length control model, and new composite control strategy were verified as correct and effective using experiments. The new composite control strategy significantly improves the motion accuracy of the end effector. Moreover, the motion control accuracy of the system is not substantially affected by changes in the virtual object's parameters. By changing the virtual object's parameters, the system can achieve training tasks such as transporting, disassembling, and anti-collision of objects of different masses.

This study provides a more realistic virtual microgravity training environment for astronauts, reduces the discomfort of astronauts in space operations, and provides new ideas for the astronauts' ground training missions. Additionally, it has good safety and economy.

In future studies, the structure of the virtual operation training system for cable-driven astronauts will be optimized to obtain increased working space. More advanced cable control algorithms will be used to further improve the system's stability.

Author Contributions: Conceptualization, F.X. and L.Z.; methodology, F.X.; software, F.X.; validation, L.Z. and Z.W.; formal analysis, Z.W. and D.S.; investigation, L.L.; resources, L.Z.; data curation, F.X.; writing—original draft preparation, F.X.; writing—review and editing, L.Z.; visualization, Z.W. and L.L.; supervision, D.S.; project administration, L.Z.; funding acquisition, L.Z. All authors have read and agreed to the published version of the manuscript.

Funding: This research was supported by the National Natural Science Foundation of China (No. 61773007).

Data Availability Statement: The data that support the findings of this study are available from the corresponding author (L.Z.) on reasonable request.

Conflicts of Interest: The authors declare no conflict of interest.

References

1. Jiang, Z.H.; Xu, J.F.; Li, H.; Huang, Q. Stable parking control of a robot astronaut in a space station based on human dynamics. *IEEE Trans. Robot.* **2020**, *36*, 399–413. [[CrossRef](#)]
2. Jamsek, M.; Kunavar, T.; Blohm, G.; Nozaki, D.; Papaxanthis, C.; White, O.; Babic, J. Effects of simulated microgravity and hypergravity conditions on arm movements in normogravity. *Front. Neural Circuit.* **2021**, *15*, 750176. [[CrossRef](#)] [[PubMed](#)]
3. Fu, Q.; Shibata, S.; Hastings, J.L.; Platts, S.H.; Hamilton, D.M.; Bungo, M.W.; Stenger, M.B.; Ribeiro, C.; Adams-Huet, B.; Levine, B.D. Impact of prolonged spaceflight on orthostatic tolerance during ambulation and blood pressure profiles in astronauts. *Circulation* **2019**, *140*, 729–738. [[CrossRef](#)] [[PubMed](#)]
4. Zhang, Y.; Richards, J.T.; Hellein, J.L.; Johnson, C.M.; Woodall, J.; Sorenson, T.; Neelam, S.; Ruby, A.M.J.; Levine, H.G. Nasa's ground-based microgravity simulation facility. *Methods Mol. Biol.* **2022**, *2368*, 281–299.
5. Sondag, A.; Dittus, H. Electrostatic positioning system for a free fall test at drop tower bremen and an overview of tests for the weak equivalence principle in past, present and future. *Adv. Space Res.* **2016**, *58*, 644–677. [[CrossRef](#)]
6. Schwartz, J.L.; Peck, M.A.; Hall, C.D. Historical review of air-bearing spacecraft simulators. *J. Guid. Control Dynam.* **2003**, *26*, 513–522. [[CrossRef](#)]

7. Zhou, M.L.; Hu, H.C.; Xu, S.H. Microgravity Simulator Based on Air Levitation for Astronauts EVA Operation Training. In Proceedings of the 3rd International Conference on Mechanical, Control, and Electronic Information (ICMCEI), Chinese Culture University, Taipei, Taiwan, China, 27–29 June 2014.
8. Brungs, S.; Egli, M.; Wuest, S.L.; Christianen, P.C.M.; van Loon, J.; Anh, T.J.N.; Hemmersbach, R. Facilities for simulation of microgravity in the ESA ground-based facility programme. *Microgravity Sci. Tec.* **2016**, *28*, 191–203. [[CrossRef](#)]
9. Sun, C.; Chen, S.Y.; Yuan, J.P.; Zhu, Z.X. A six-dof buoyancy tank microgravity test bed with active drag compensation. *Microgravity Sci. Tec.* **2017**, *29*, 391–402. [[CrossRef](#)]
10. Wang, T.; You, Z.H.; Song, W.; Zhu, S.Q. Dynamic analysis of an underwater cable-driven manipulator with a fluid-power buoyancy regulation system. *Micromachines* **2020**, *11*, 1042. [[CrossRef](#)]
11. Macaluso, T.; Bourdin, C.; Buloup, F.; Mille, M.L.; Sainton, P.; Sarlegna, F.R.; Taillebot, V.; Vercher, J.L.; Weiss, P.; Bringoux, L. Kinematic features of whole-body reaching movements underwater: Neutral buoyancy effects. *Neuroscience* **2016**, *327*, 125–135. [[CrossRef](#)] [[PubMed](#)]
12. Zang, W.S.; Chen, X.; Zhao, J. Multi-disturbance observers-based nonlinear control scheme for wire rope tension control of hoisting systems with backstepping. *Actuators* **2022**, *11*, 321. [[CrossRef](#)]
13. Babaghasabha, R.; Khosravi, M.A.; Taghirad, H.D. Adaptive robust control of fully-constrained cable driven parallel robots. *Mechatronics* **2015**, *25*, 27–36. [[CrossRef](#)]
14. Danhe, C.; Koryanov, V.V. The Study of the Dynamics of the Spacecraft Landing on a Celestial Body with Microgravity Under Different Fixing Conditions. In Proceedings of the International Conference on Measurement Instrumentation and Electronics (ICMIE), Munich, Germany, 6–8 June 2016.
15. Faure, C.; Fortin-Cote, A.; Robitaille, N.; Cardou, P.; Gosselin, C.; Laurendeau, D.; Mercier, C.; Bouyer, L.; McFadyen, B.J. Adding haptic feedback to virtual environments with a cable-driven robot improves upper limb spatio-temporal parameters during a manual handling task. *IEEE Trans. Neur. Sys. Reh.* **2020**, *28*, 2246–2254. [[CrossRef](#)]
16. Lambert, P.; Da Cruz, L.; Bergeles, C. Design, modeling, and implementation of a 7-dof cable-driven haptic device with a configurable cable platform. *IEEE Robot. Autom. Let.* **2020**, *5*, 5764–5771. [[CrossRef](#)]
17. Salamon, N.; Grimm, J.M.; Horack, J.M.; Newton, E.K. Application of virtual reality for crew mental health in extended-duration space missions. *Acta Astronaut.* **2018**, *146*, 117–122. [[CrossRef](#)]
18. Gouttefarde, M.; Lamaury, J.; Reichert, C.; Bruckmann, T. A versatile tension distribution algorithm for n-dof parallel robots driven by n+2 cables. *IEEE Trans. Robot.* **2015**, *31*, 1444–1457. [[CrossRef](#)]
19. Mousavi, M.R.; Ghanbari, M.; Moosavian, S.A.A.; Zarafshan, P. Rapid and safe wire tension distribution scheme for redundant cable-driven parallel manipulators. *Robotica* **2022**, *40*, 2395–2408. [[CrossRef](#)]
20. Meziane, R.; Cardou, P.; Otis, M.J.D. Cable interference control in physical interaction for cable-driven parallel mechanisms. *Mech. Mach. Theory* **2019**, *132*, 30–47. [[CrossRef](#)]
21. Zou, Y.P.; Wu, X.S.; Zhang, B.L.; Zhang, Q.; Zhang, A.D.; Qin, T. Stiffness analysis of parallel cable-driven upper limb rehabilitation robot. *Micromachines* **2022**, *13*, 253. [[CrossRef](#)]
22. Li, L.L.; Zhang, L.X.; Wang, B.; Xue, F.; Zou, Y.P.; Song, D. Running experimental research of a cable-driven astronaut on-orbit physical exercise equipment. *Machines* **2022**, *10*, 377. [[CrossRef](#)]
23. Xue, F.; Zhang, L.X.; Wang, C.; Wang, Z.H.; Fan, Y.H. Research on Structure Design and Control of Plane 3-DOF Cable Driven Virtual Microgravity Training System. In Proceedings of the 12th International Conference on CYBER Technology in Automation, Control, and Intelligent Systems (CYBER 2022), Baishan, China, 27–31 July 2022.
24. Fortin-Cote, A.; Cardou, P.; Gosselin, C. An Admittance Control Scheme for Haptic Interfaces Based on Cable-Driven Parallel Mechanisms. In Proceedings of the IEEE International Conference on Robotics and Automation (ICRA), Hong Kong, China, 31 May–7 June 2014.
25. Park, J.H.; Kim, M.C.; Bohl, R.; Gommel, S.A.; Kim, E.S.; Choi, E.; Park, J.O.; Kim, C.S. A portable intuitive haptic device on a desk for user-friendly teleoperation of a cable-driven parallel robot. *Appl. Sci.* **2021**, *11*, 3823. [[CrossRef](#)]
26. Song, D.; Zhang, L.X.; Xue, F. Configuration optimization and a tension distribution algorithm for cable-driven parallel robots. *IEEE Access* **2018**, *6*, 33928–33940. [[CrossRef](#)]
27. Wang, L.; Lin, L.J.; Chang, Y.; Song, D. Velocity planning for astronaut virtual training robot with high-order dynamic constraints. *Robotica* **2020**, *38*, 2121–2137. [[CrossRef](#)]
28. Li, L.L.; Zhang, L.X.; Wang, B.; Song, D. Simulation Analysis of a Cable-Driven Astronaut on-Orbit Physical Exercise Equipment. In Proceedings of the 9th International Conference on Automation, Robotics and Applications (ICARA), Abu Dhabi, United Arab Emirates, 10–12 February 2023.
29. Ferravante, V.; Riva, E.; Taghavi, M.; Braghin, F.; Bock, T. Dynamic analysis of high precision construction cable-driven parallel robots. *Mech. Mach. Theory* **2019**, *135*, 54–64. [[CrossRef](#)]
30. Xing, E.Z.; Zhou, C.Y. Analysis of the bending behavior of a cable structure under microgravity. *Int. J. Mech. Sci.* **2016**, *114*, 132–140. [[CrossRef](#)]
31. Rushton, M.; Jamshidifar, H.; Khajepour, A. Multiaxis reaction system (MARS) for vibration control of planar cable-driven parallel robots. *IEEE Trans. Robot.* **2019**, *35*, 1039–1046. [[CrossRef](#)]
32. Rijk, R.D.; Rushton, M.; Khajepour, A. Out-of-plane vibration control of a planar cable-driven parallel robot using a multiaxis reaction system. *IEEE-ASME Trans. Mech.* **2018**, *23*, 1684–1692. [[CrossRef](#)]

33. Kraus, W.; Schmidt, V.; Rajendra, P.; Pott, A. System Identification and Cable Force Control for a Cable-Driven Parallel Robot with Industrial Servo Drives. In Proceedings of the IEEE International Conference on Robotics and Automation (ICRA), Hong Kong, China, 31 May–7 June 2014.
34. Song, D.; Xiao, X.L.; Li, G.; Zhang, L.X.; Xue, F.; Li, L.L. Modeling and control strategy of a haptic interactive robot based on a cable-driven parallel mechanism. *Mech. Sci.* **2023**, *14*, 19–32. [[CrossRef](#)]
35. Hussein, H.; Santos, J.C.; Izard, J.B.; Gouttefarde, M. Smallest maximum cable tension determination for cable-driven parallel robots. *IEEE Trans. Robot.* **2021**, *37*, 1186–1205. [[CrossRef](#)]
36. Chawla, I.; Pathak, P.M.; Notash, L.; Samantaray, A.K.; Li, Q.G.; Sharma, U.K. Inverse and forward kineto-static solution of a large-scale cable-driven parallel robot using neural networks. *Mech. Mach. Theory* **2023**, *179*, 105107. [[CrossRef](#)]
37. Chen, Q.; Zi, B.; Sun, Z.; Li, Y.; Xu, Q.S. Design and development of a new cable-driven parallel robot for waist rehabilitation. *IEEE-ASME Trans. Mech.* **2019**, *24*, 1497–1507. [[CrossRef](#)]
38. Yuan, H.; Courteille, E.; Deblaise, D. Static and dynamic stiffness analyses of cable-driven parallel robots with non-negligible cable mass and elasticity. *Mech. Mach. Theory* **2015**, *85*, 64–81. [[CrossRef](#)]
39. Gonzalez-Rodriguez, A.; Martin-Parra, A.; Juarez-Perez, S.; Rodriguez-Rosa, D.; Moya-Fernandez, F.; Castillo-Garcia, F.J.; Rosado-Linares, J. Dynamic model of a novel planar cable driven parallel robot with a single cable loop. *Actuators* **2023**, *12*, 200. [[CrossRef](#)]
40. Juarez-Perez, S.; Martin-Parra, A.; Arena, A.; Ottaviano, E.; Gattulli, V.; Castillo-Garcia, F.J. Dynamic control of a novel planar cable-driven parallel robot with a large wrench feasible workspace. *Actuators* **2022**, *11*, 367. [[CrossRef](#)]
41. Wang, Y.L.; Wang, K.Y.; Zhang, Z.X.; Han, Z.; Wang, W.L. Analysis of dynamical stability of rigid-flexible hybrid-driven lower limb rehabilitation robot. *J. Mech. Sci. Technol.* **2020**, *34*, 1735–1748. [[CrossRef](#)]

Disclaimer/Publisher’s Note: The statements, opinions and data contained in all publications are solely those of the individual author(s) and contributor(s) and not of MDPI and/or the editor(s). MDPI and/or the editor(s) disclaim responsibility for any injury to people or property resulting from any ideas, methods, instructions or products referred to in the content.